An estimate of the cross-frontal transport at the shelf break of the East China Sea with the Finite Volume Coastal Ocean Model

Atsuhiko Isobe[1] and Robert C. Beardsley[2]

Received 12 September 2005; revised 21 November 2005; accepted 27 December 2005; published 23 March 2006.

[1] The Finite Volume Coastal Ocean Model (FVCOM) is used to estimate the onshore cross-frontal transport at the shelf break of the East China Sea. Boundary conditions of FVCOM are provided by the Princeton Ocean Model simulating ocean currents in the Yellow Sea and East China Sea realistically. One advantage of this study is that the unstructured triangular cell grid of FVCOM resolves complex bottom topography that may trigger Kuroshio frontal waves. It is anticipated that these nonlinear frontal waves enhance the exchange of seawater between the Kuroshio and shelf regions. Kuroshio frontal waves in the model are excited around the location where the bottom slope changes abruptly, and have the phase speed and amplitude consistent with those observed in the East China Sea. In addition, the model reproduces the onshore transport associated with growing frontal waves in the upper and lower layers. On the basis of passive tracer experiments, the annually averaged onshore-transport integrated along the shelf break is estimated to be 0.85×10^6 m^3/s.

Citation: Isobe, A., and R. C. Beardsley (2006), An estimate of the cross-frontal transport at the shelf break of the East China Sea with the Finite Volume Coastal Ocean Model, *J. Geophys. Res.*, *111*, C03012, doi:10.1029/2005JC003290.

1. Introduction

[2] It is reasonable to consider the water exchange induced by Kuroshio frontal waves (or frontal eddies) growing at the shelf break in the East China Sea; see Figure 1 for the topography and schematic view of ocean currents. In fact, on the basis of field measurements and numerical modeling, *Isobe et al.* [2004] demonstrate that Kuroshio frontal waves cause offshore intrusions of less-saline shelf water into the Kuroshio intermediate layer. However, the offshore transport across the shelf break occurs mostly when the Kuroshio on the shelf turns toward the Tokara Strait. Hence it is unlikely that the eddy-induced offshore transport is a significant fraction in the water budget in this area.

[3] This study attempts to estimate the total amount of the onshore cross-frontal (or cross-shelf) transport induced by nonlinear frontal waves at the shelf break of the East China Sea; the shelf break is located around the 200-m isobath in this area. We here consider a box model representing the East China Sea shelf in a steady state. Integrating the salinity conservation equation over the box model yields

$$0 \cdot Q_R + S_{TW} \cdot Q_{TW} + S_{KS} \cdot Q_{KS} + (S_{KS} - S_{ES}) \cdot Q = S_{TS} \cdot Q_{TS}, \quad (1)$$

where S_{TW}, S_{KS}, S_{ES}, and S_{TS} denote salinities at the Taiwan Strait, Kuroshio upper layer, East China Sea shelf, and Tsushima/Korea Strait, respectively. Q_R, Q_{TW}, Q_{KS}, and Q_{TS} represent the river discharge into the area, the volume transport through the Taiwan Strait, the onshore transport from the Kuroshio across the shelf break, and volume transport through the Tsushima/Korea Strait, respectively. As mentioned above, the objective of this study is to estimate Q, that is, the onshore (= offshore) cross-frontal transport associated with the water exchange at the shelf break. Note that the freshwater flux through the sea surface is negligible in a long-term average [*Chen et al.*, 1994]. The above volume transports must satisfy the below equation:

$$Q_R + Q_{TW} + Q_{KS} = Q_{TS}. \quad (2)$$

Shen et al. [1998] estimate Q_R to be 0.03 Sv (Sverdrups, 1 Sv = 10^6 m^3/s) derived mostly from the Changjiang. Q_{TW} and Q_{TS} have been estimated to be 1.60 Sv [*Zhao and Fang*, 1991] and 2.40 Sv [*Isobe et al.*, 2002], respectively, and so we can deduce Q_{KS} to be 0.77 Sv. In addition, averaging salinity data archived in the World Ocean Atlas 1994 (WOA94 [*Boyer and Levitus*, 1994]), we can determine the salinity at the Taiwan Strait (S_{TW}) to be 33.93, the salinity in the Kuroshio upper layer (S_{KS} east of Taiwan [see *Isobe et al.*, 2002]) to be 34.57, the salinity over the East China Sea shelf (S_{ES}) to be 33.85, and the salinity at the Tsushima/Korea Strait (S_{TS}) to be 34.03, respectively. Substituting these values into the equation (1) leads to the onshore cross-frontal transport (Q) of 1.06 Sv. Recently, on the basis of a numerical modeling, *Wu and Hsin* [2005] indicate that the winter transport through the Taiwan Strait has been overestimated, and that the annually-averaged transport is estimated to be 1.09 Sv. Nevertheless, our rough estimate

[1]Department of Earth System Science and Technology, Interdisciplinary Graduate School of Engineering Sciences, Kyushu University, Kasuga, Japan.
[2]Physical Oceanography Department, Woods Hole Oceanographic Institution, Woods Hole, Massachusetts, USA.

0148-0227/06/2005JC003290$09.00

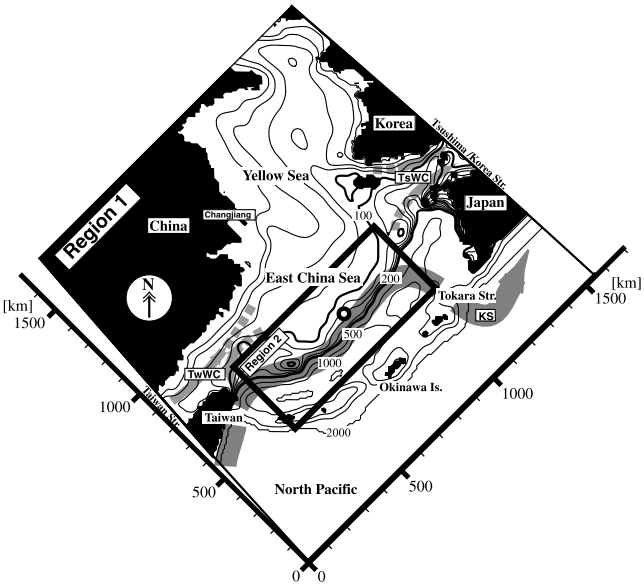

Figure 1. Model domain of Region 1. Also shown are isobaths in meters based on ETOPO 5 data set. Contour interval is 20 m except for isobaths of 500, 1000, and 2000 m. The rectangle represents the model domain of Region 2 that is enlarged later in Figure 4. The open circle denotes the JMA buoy station. Ocean currents in this area are shown schematically by gray arrows. The Kuroshio, Taiwan Warm Current, and Tsushima Warm Current are represented by letters, KS, TwWC, and TsWC, respectively. Paths for the latter two currents change to dashed lines, and disappear in the central part of the East China Sea to express the fact that the origin of the Tsushima Warm Current is still a question of debate [*Uda*, 1934; *Fang et al.*, 1991; *Lie and Cho*, 1994; *Lie et al.*, 1998; *Hsueh et al.*, 1996; *Katoh et al.*, 1996; *Katoh et al.*, 2000; *Isobe*, 1999a, 1999b, 2000].

suggests that the onshore cross-frontal transport ($Q = 0.61$ Sv) is comparable with volume transports (i.e., Q_{TS} and Q_{TW}) of ocean currents over the shelf. Moreover, this transport is much larger than the river discharge into the area.

[4] Is this onshore transport really comparable with the volume transport of ocean currents over the shelf? If this is the case, the cross-frontal transport at the shelf break must be critical to determine water mass characteristics of the shelf circulation in the East China Sea. This scenario is consistent with *Lim* [1971] and *Sawara and Hanzawa* [1979] who point out, on the basis of archived hydrographic data, that the water mass of the Tsushima Warm Current is formed by a mixture between Kuroshio and shelf waters around the shelf break. Is the onshore transport induced by eddies much larger than the river discharge of the Changjiang that is a prominent nutrient source in this area? If this is the case, the cross-frontal onshore transport from the nutrient-rich subsurface layer may be the most prominent nutrient source in this area. This scenario is consistent with *Chen and Wang* [1999] who argue, on the basis of a nutrient budget in this area, that the onshore transport from the Kuroshio subsurface layer is a major source of nutrients to the East China Sea shelf.

[5] Difficulty arises from intense spatiotemporal variability of frontal waves in estimating the cross-shelf transport along the entire East China Sea shelf break. A snapshot of the transport might be observed when one encounters a frontal wave by chance [e.g., *Yanagi et al.*, 1998]. However, it is probably impossible to estimate the total amount of the transport integrated over the shelf break only on the basis of field measurements. Hence it is reasonable to use a numerical model approach in which Kuroshio frontal waves are reproduced accurately.

[6] The numerical model in this study is required to simulate the large-scale ocean circulation realistically in the study area; otherwise, a wrong Kuroshio structure results in frontal-wave characteristics different from those observed in this area. Thereby the modeling should be carried out in a broad domain with boundary conditions consistent with observations. In addition, the model is required to simulate Kuroshio frontal waves realistically in order to quantify their contribution to the cross-frontal onshore transport. Thereby the model must include small-scale topographic irregularity that may trigger frontal waves. In this study, two numerical models are combined to satisfy these two requirements.

[7] One is the Princeton Ocean Model (hereinafter, POM [*Mellor*, 2003]) that has been used widely in shelf circulation studies. As shown later, this model reproduces the overall current features satisfactory in Region 1 of Figure 1. The second model is the Finite Volume Coastal Ocean Model (hereinafter, FVCOM [*Chen et al.*, 2003]), which is adopted for a limited area (Region 2 of Figure 1) around the shelf break. FVCOM uses a horizontal grid composed of unstructured triangular cells that allow topographic irregularities to be resolved precisely. In the present application, results of POM are given to FVCOM as boundary conditions updated every time step (i.e., one-way nested model). In general, finite-volume models (e.g., FVCOM) need a calculation time longer than finite difference models (e.g., POM); for instance, the external mode (see *Chen et al.* [2003] for its meaning) of FVCOM is solved using the fourth-order Runge-Kutta scheme that requires four time-iterations in each time step in order to enhance the model accuracy instead of the single time step used in POM. However, we will be able to model the large-scale circulation efficiently because of POM used for the large area. In addition to the large-scale circulation, as shown later, the combination of these two models reproduces frontal waves realistically at the shelf break in the East China Sea, and enables us to estimate the onshore cross-frontal transport throughout a year.

[8] This paper is organized as follows. Section 2 describes observed characteristics of the Kuroshio frontal wave that is a target to be reproduced in our numerical model. Model details are provided in section 3. Model results and comparison with observations are shown in section 4. In section 5, we demonstrate examples of the eddy-induced cross-frontal transport at the shelf break, and estimate the onshore cross-frontal transport integrated along the entire shelf break in our numerical model. Section 6 gives the conclusion.

2. Kuroshio Frontal Waves Observed at a Buoy Station

[9] The Kuroshio frontal wave has been investigated by many authors on the basis of mooring data [*Sugimoto et al.*,

Table 1. Characteristics of the Kuroshio Frontal Wave Obtained in Previous Studies

References	Periods, Days	Wavelength, km	Phase Velocity, km/d
Sugimoto et al. [1988]	11–14	300–350	26
Qiu et al. [1990]	14–20	100–150	17–22
Ichikawa and Beardsley [1993]	8–23	150–375	8–19
James et al. [1999]	11	217	20

1988; *Qiu et al.*, 1990; *James et al.*, 1999], satellite IR images [*Qiu et al.*, 1990], and archived hydrographic and current data [*Ichikawa and Beardsley*, 1993]. The period, wavelength, and phase speed have been found to be between 8 and 23 days, 100 and 375 km, and 8 and 26 km/day, respectively (Table 1). Here we also describe characteristics of the frontal wave using temperature records obtained at a long-term buoy station. The Japan Meteorological Agency (hereinafter, JMA) had monitored water temperatures at 2, 20, and 50 m at the buoy station (126°20′E, 28°10′N; 126-m depth) shown by the open circle in Figure 1; *Qiu et al.* [1990] also used temperature records from this buoy station.

[10] Figure 2 shows time series of temperature at 20-m depth from 1995 to 2000. These time series represent anomalies from each annual mean. In addition, we remove annual variations by fitting a sinusoidal curve to focus on variations with periods much shorter than the annual cycle, and remove short-term fluctuations due to meteorological disturbances using a 5-day running mean. Periodicity of the above processed data is investigated with wavelet analysis [*Torrence and Compo*, 1998]. Figure 3 shows wavelet spectra of 2-, 20-, and 50-m temperature records. Also shown are spectra averaged in each period on the right-hand side of these panels.

[11] In Figure 2 we find large fluctuations with periods less than one month and amplitudes around 1 to 2°C. Figure 3 shows that strong signals are observed in the period band of Kuroshio frontal waves although the upper limit seems to extend beyond 30 days. *Qiu et al.* [1990] point out that these short-term (i.e., less than 1 month) fluctuations are caused by the passing of frontal waves at the buoy station. Signals are weak during summer in the wavelet spectrum at 2-m depth. However, apart from the surface layer, short-term fluctuations are visible regardless of season. This is because the horizontal gradient of the sea surface temperature weakens owing to intense surface heating in summer, and because horizontal motion related to frontal waves is difficult to detect in the temperature distribution at 2-m depth.

[12] Beside the short-term fluctuations caused by the passing of frontal waves, relatively strong signals are also found with periods longer than several months (see arrows in Figure 3). We hereinafter call these signals "semiannual variation" for convenience although, in strict terms, the period seems to vary between 90 and 200 days. This variation will be useful to prove model accuracy as shown later in section 4, although the dynamical interpretation for

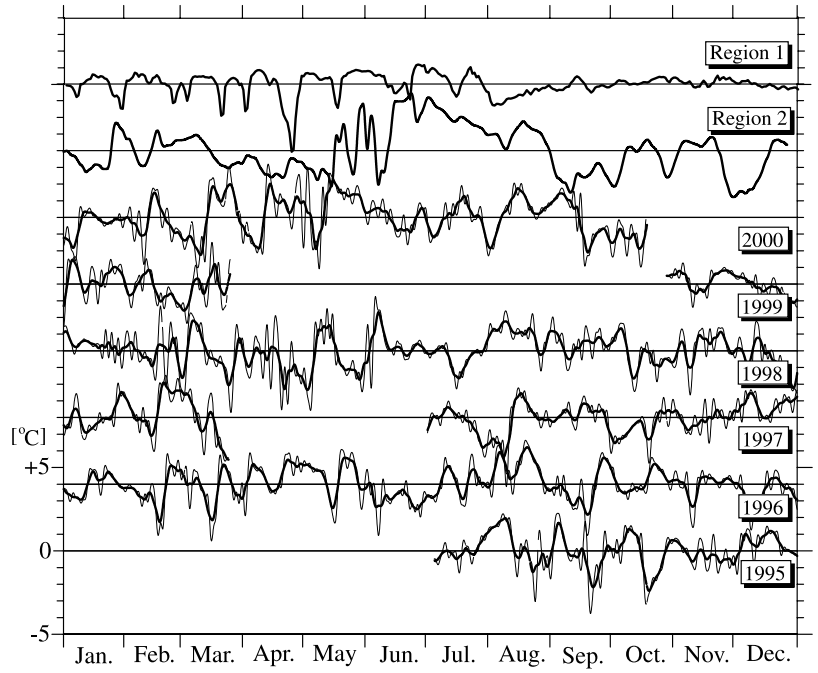

Figure 2. Time series of temperature at the JMA buoy station from 1995 to 2000. Data at 20-m depth are used here. All time series denote anomalies from each annual mean represented by abscissas. In addition, the annual variation is removed from each time series. Thin lines denote hourly data smoothed with a 48-hour low-pass filter [*Hanawa and Mitsudera*,1985]. In addition, the fluctuations due to meteorological disturbances are smoothed with a 5-day running mean as shown by thick lines. Curves are interrupted when data are missing. Upper two lines denote time series at the buoy station in each numerical model (see section 4.2).

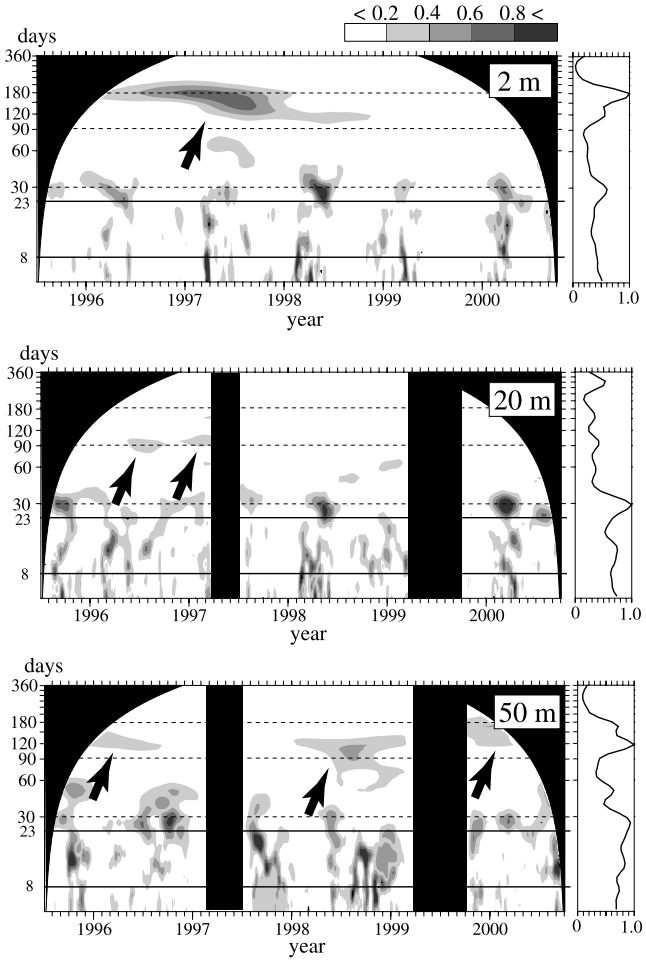

Figure 3. Wavelet spectra for temperature time series at 2-, 20-, and 50-m depths. The abscissa of each panel represents the time, and the ordinate denotes the period in days. The magnitude of each spectrum is normalized by the variance of that time series, and is indicated by the gray scale shown in the upper right of this figure. Wavelet spectra cannot be computed on either end because of the finite-length time series [see *Torrence and Compo*, 1998], and so the area is blacked out. The upper and lower limits of the periods in Table 1 are shown by the two horizontal lines in each panel. Arrows indicate the "semiannual" variation; see the text for details. Also shown are spectra averaged in each period on the right-hand side of the panels. These averaged spectra are normalized by the maximum value in each panel.

the semiannual variation is not the main subject of this study.

3. Model Descriptions

3.1. POM Adopted for Region 1

[13] POM is adopted for Region 1 covering the Yellow Sea, the East China Sea, and a part of the North Pacific as shown in Figure 1. The grid spacing is 1/12 degree (~9 km) in latitude and longitude. We use the topographic data set with 1/12-degree resolution (ETOPO5) provided by the U.S. National Geophysical Data Center. The model domain is divided into 11 σ-layers vertically.

[14] The horizontal viscosity and diffusivity are parameterized with the Smagorinsky diffusion formula provided in the original POM code. The vertical viscosity and diffusivity are obtained through the second-order turbulence closure scheme of *Mellor and Yamada* [1982]. Parameters used in this model are listed in Table 2.

[15] Observed volume transports are imposed at the Taiwan Strait [*Zhao and Fang*, 1991], the Tsushima/Korea Straits [*Isobe et al.*, 2002], east of Taiwan, and south of Japan. The latter two denote Kuroshio transports determined in line with the estimate of *Ichikawa and Chaen* [2000]. In addition, the temperature and salinity at each open boundary are determined with climatological values archived in WOA94. The vertical gradient of the current velocity is specified at each open boundary so that geostrophy is satisfied on the basis of hydrographic data in WOA94. Using the wind speed in the Comprehensive Ocean-Atmosphere Data Set [*Woodruff et al.*, 1987], we compute the wind stress at each grid using the neutral drag coefficient of *Large and Pond* [1981]. The heat flux through the sea surface is given by the sea surface temperature restored to climatological values (WOA94) within a timescale much shorter than the seasonal variation; we choose 5 days in this application. A homogeneous freshwater flux is prescribed at the sea surface over the whole model domain. This value is the difference between the evaporation and precipitation averaged spatially in the Yellow and East China seas [*Chen et al.*, 1994]. Fresh water from the Changjiang [*Shen et al.*, 1998] is also supplied to the model. The above boundary conditions and forcing vary with an annual cycle. Time integration is continued until the end of year 8 when year-to-year variability disappears. Results taken from final two years are used in subsequent calculations.

[16] Results in Region 1 have already been presented by *Chang and Isobe* [2003]. This model reproduced the behavior of Changjiang Diluted Water accurately (see their

Table 2. Parameters Used in Numerical Models

Parameters	Region 1 (POM)	Region 2 (FVCOM)
Coefficient for Smagorinsky diffusivity[a]	0.08	0.16
Grid spacing, degree	1/12	1/30–1/12
(Layer thickness/depth) from the top layer	0.01563, 0.01563, 0.03125, 0.0625, 0.125, 0.125, 0.125, 0.125, 0.125, 0.125	same as in Region 1 (POM)
External mode time step,[b] s	20	24
Internal mode time step,[b] s	600	240

[a]Referred to as "HORCON" in the original code of *Mellor* [2003].
[b]See *Mellor* [2003] for the meaning of "external" and "internal" modes.

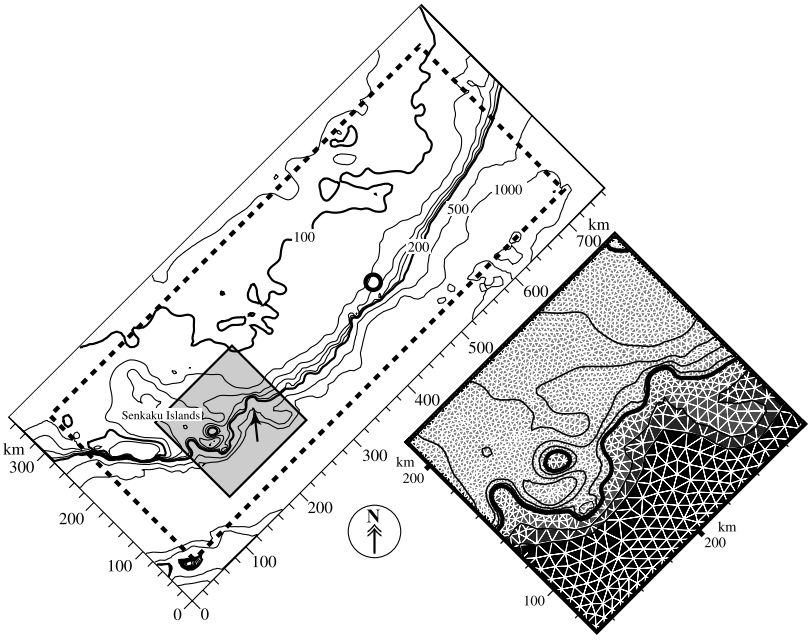

Figure 4. Model domain of Region 2. Also shown are isobaths based on the data set of *Choi et al.* [2002]. Contour interval is 20 m except for the 500- and 1000-m isobaths. The dashed line denotes the boundary between the model domain and sponge region. The open circle represents the JMA buoy station. The area within the stippled square near Senkaku Islands is enlarged in the lower right panel to illustrate the unstructured triangular grid cells of FVCOM depicted with white lines. The arrow indicates the area where the bottom slope changes abruptly (see the text for details).

Figures 6 and 7) and the freshwater transport at the Tsushima/Korea Straits (see their Figure 9) as observed by *Isobe et al.* [2002]. We refer the reader to *Chang and Isobe* [2003] for a more thorough description of model details.

3.2. FVCOM Adopted for Region 2

[17] Region 2 is located over the shelf break as shown in Figure 1. The areas where the Kuroshio impinges on the shelf break east of Taiwan and where the Kuroshio turns abruptly toward the Tokara Strait are omitted in Region 2 to avoid the complexity of currents at the boundaries between the two numerical models. Thus one may find the Kuroshio flowing parallel to the shelf break in the model results in Region 2. However, the cross-shelf transport integrated along the entire shelf break must be offshore because part of the Kuroshio running over the shelf has to leave for the Tokara Strait. Nevertheless, onshore cross-shelf transport exists owing to growing frontal waves as shown later in section 5. As mentioned previously, FVCOM is adopted for Region 2 to resolve the complex bottom topography using unstructured triangular grid cells. The bathymetric data set of *Choi et al.* [2002] with the 1/60-degree resolution is used for Region 2. This data set provides us with one of the most accurate and high-spatial resolution bathymetric grid data in the East Asian marginal seas.

[18] Figure 4 shows the topography of Region 2 and illustrates the FVCOM triangular-cell in one region of complex topography over the shelf break. Note that the shelf break topography indicated by the arrow (see Figure 4) features a complex indentation, and that the bottom slope changes abruptly there. We will show that this topographic irregularity forces fluctuations (section 4.2) as well as the stable eddy (section 4.1). The length of cell edges is the same as that of Region 1 (1/12 degree) at open boundaries so that Region 2 is connected to Region 1 without spatial interpolations of variables. Thereby the one-way nested model in this study is likely to conserve the volume transport between two different models. The length reduces to 1/30 degree ($\sim$3 km) near the shelf break, which is sufficiently small to reproduce frontal waves with a wavelength between 100 and 375 km. The model domain is divided into 11 σ-layers in Region 2 in the same manner as Region 1.

[19] FVCOM uses the Smagorinsky formula for the horizontal viscosity and diffusivity. In addition, the same scheme and parameters used in Region 1 for the vertical viscosity and diffusivity are used in FVCOM. Parameters used for FVCOM are listed in Table 2.

[20] When modeling Region 1 during the final two years, we save horizontal current velocities, temperature, and salinity along the Region 2 boundaries once each day. These daily variables are then smoothed with a 5-day running mean to remove higher frequency disturbances. These smoothed data are updated every FVCOM time step using linear interpolation and used as the Region 2 boundary conditions.

[21] Areas within 40 km of the Region 2 boundaries are "sponge regions," where horizontal current velocities, temperature, salinity, and sea surface elevation in Region 2 are restored to those of Region 1 to suppress artificial disturbances that might arise owing to the connection between the two different models. These variables in Region 1 are saved once each day in the final two years, smoothed with a 5-day running mean, and then updated at each FVCOM time step using linear interpolation prior to spatial conversion. We add a simple nudging term, $\gamma(f_1 - f_2)$, to the continuity equation and conservation equations for momentum, temperature and salinity. Here γ is the reciprocal of the nudging

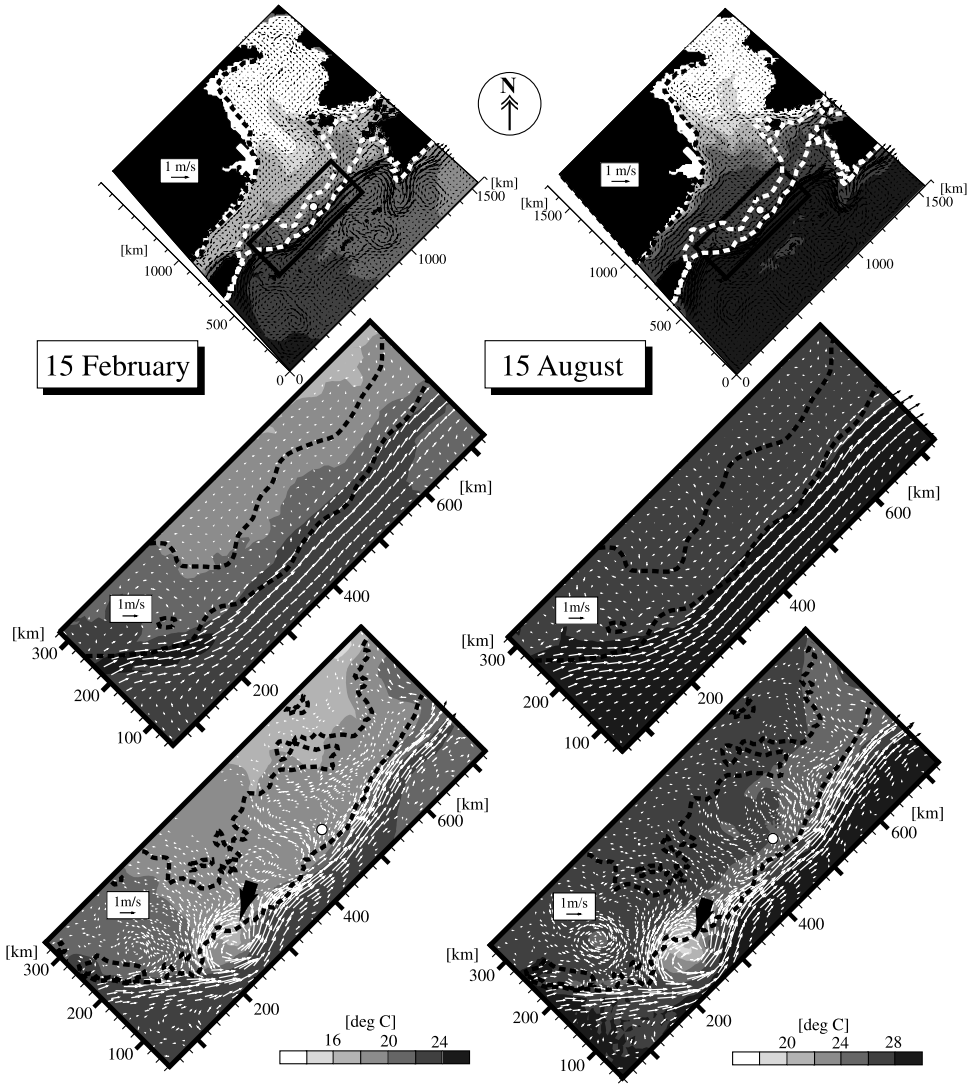

Figure 5. Modeled currents and temperature at 10-m depth on (left) 15 February and (right) 15 August. Top two panels indicate results of Region 1. The area within the rectangle is enlarged in middle two panels. Bottom two panels represent results of Region 2. The arrow points to a cyclonic eddy existing stably at the shelf break. The open circle in the bottom panels denotes the JMA buoy station. The 100- and 200-m isobaths are depicted in middle and bottom panels with dashed lines. Current vectors are depicted every third grid, second grid, and fourth cell nodes in the top, middle, and bottom panels, respectively. The temperature is indicated by the gray scale shown at the bottom of this figure. Note that different gray scales are used for the temperature distributions in February and August. The sponge region is omitted in middle and bottom panels.

timescale, f_1 and f_2 denote variables in Regions 1 and 2, respectively. The definition point of f_1 is converted to that of f_2 with a Gaussian filter whose e-folding scales are adjusted to the lengths of the triangular cell edges at each definition point. The timescale of the nudging is 3 hours at the boundary. The nudging coefficient decreases linearly toward the model interior, and becomes zero at $\geq$40-km distances from the boundaries. In order to make bathymetric data in the sponge region, ETOPO5 is blended with data from *Choi et al.* [2002] through a weighted average whose coefficient varies linearly from 0 to 1 with the distance from boundaries.

[22] Heat, freshwater and momentum fluxes through the Region 2 sea surface are the same as those in Region 1. Definition points of the wind stress and restoring temperature are adjusted with the same Gaussian filter as variables in the sponge region.

[23] FVCOM is integrated through the end of the second year when the short-term fluctuations of the modeled variables appear to be in quasi-steady state. Results taken from the final year are used in subsequent analyses.

4. Results

4.1. Snapshots of the Modeled Ocean

[24] Figure 5 shows snapshots of current vectors and temperature at 10-m depth on 15 February (representative of midwinter) and 15 August (midsummer). Results in

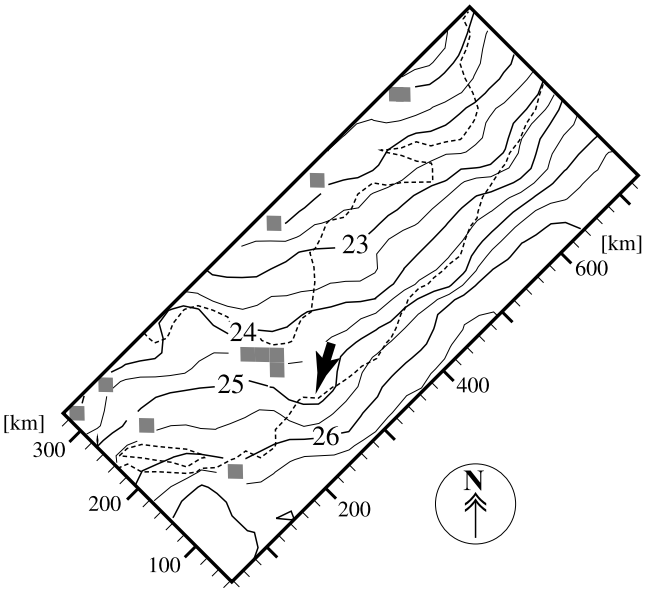

Figure 6. Horizontal distribution of the climatological temperature observed at 10-m depth in the same area as the middle and bottom panels of Figure 5. The 100- and 200-m isobaths are depicted with dashed lines. The arrow points to a cyclonic eddy at the shelf break. Stippled rectangles indicate grids where the number of temperature data is less than 20.

Region 1 are shown in the top panels. The area within the rectangle in the top panels is enlarged in the middle two panels to emphasize the Kuroshio currents near the shelf break. Comparing the modeled behavior of the Changjiang river plume with that observed, *Chang and Isobe* [2003] showed that the POM (i.e., Region 1) reproduces the general structure of the currents over the shelf accurately. In these two middle panels, the Kuroshio mainstream is located on the offshore side of the 200-m isobath (i.e., along the shelf break) with a current speed of about 1 m/s. The path and current speed are consistent with the Kuroshio observed in this area; see *Qiu et al.* [1990] for the long-term mean current field. However, in the middle two panels, the Kuroshio flows smoothly along the shelf break without remarkable eddy activity.

[25] When POM within the rectangle is replaced by the high-resolution FVCOM (i.e., Region 2) as shown in the bottom two panels, the Kuroshio mainstream is still located along the shelf break, but exhibits significant spatial variability associated with the more complex local bathymetry. The most remarkable difference between the two model solutions is eddies revealed at the shelf break. In particular, a cyclonic eddy (see the large arrow) exists in both the FVCOM February and August snapshots near the area with the complex indentation. Figure 6 shows a climatological distribution of temperature observed at 10-m depth. To depict this figure, we use expendable bathythermograph data provided on the web site of Japan Oceanographic Data Center (http://www.jodc.go.jp/) in addition to the data archived in WOA94. All data (258,764 data in total) are averaged in each grid with the 10-min resolutions in latitude and longitude after removing the seasonal variation by fitting an annual sinusoidal curve. A cyclonic eddy (see the large arrow) is detected at the location where the cyclonic eddy appears in the FVCOM snapshots.

4.2. Fluctuations Revealed in Models

[26] The top panel of Figure 7 shows the horizontal distribution of the root mean square (RMS) of temperature at 10-m depth in the final year in Region 2. RMS is defined as $\sqrt{\sum (T-\overline{T})^2/N}$ at each FVCOM temperature node, where T is the temperature after removing the seasonal variation by fitting an annual sinusoidal curve, $\overline{T}$ the annual mean at each node, and N the number of time steps in a year. The areas with large RMS appear along the shelf break and broaden in the Kuroshio downstream direction. This distribution pattern of RMS suggests that frontal waves grow

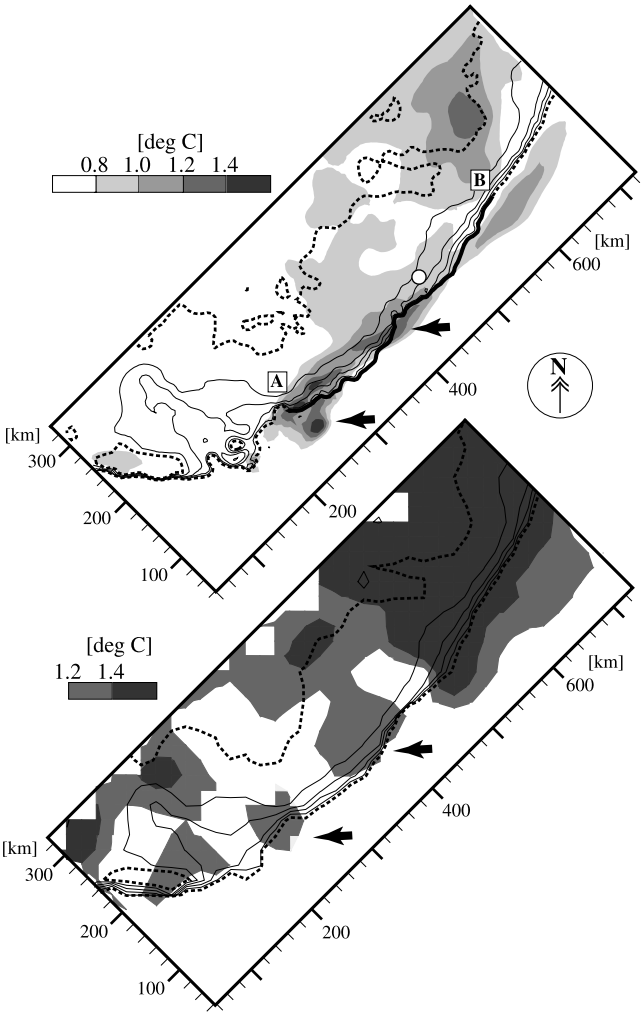

Figure 7. Horizontal distribution of the root mean square of temperature at 10-m depth in the (top) model and (bottom) observation. The magnitude is indicated by the gray scale. Also shown are isobaths between the 100-m and 200-m isobaths (dashed lines) with an interval of 20 m. In the top panel, the bold solid line denotes the 200-m isobath between points *A* and *B* along which space-time plots of temperature are depicted in the following figures. The open circle denotes the JMA buoy station. The sponge layer is omitted.

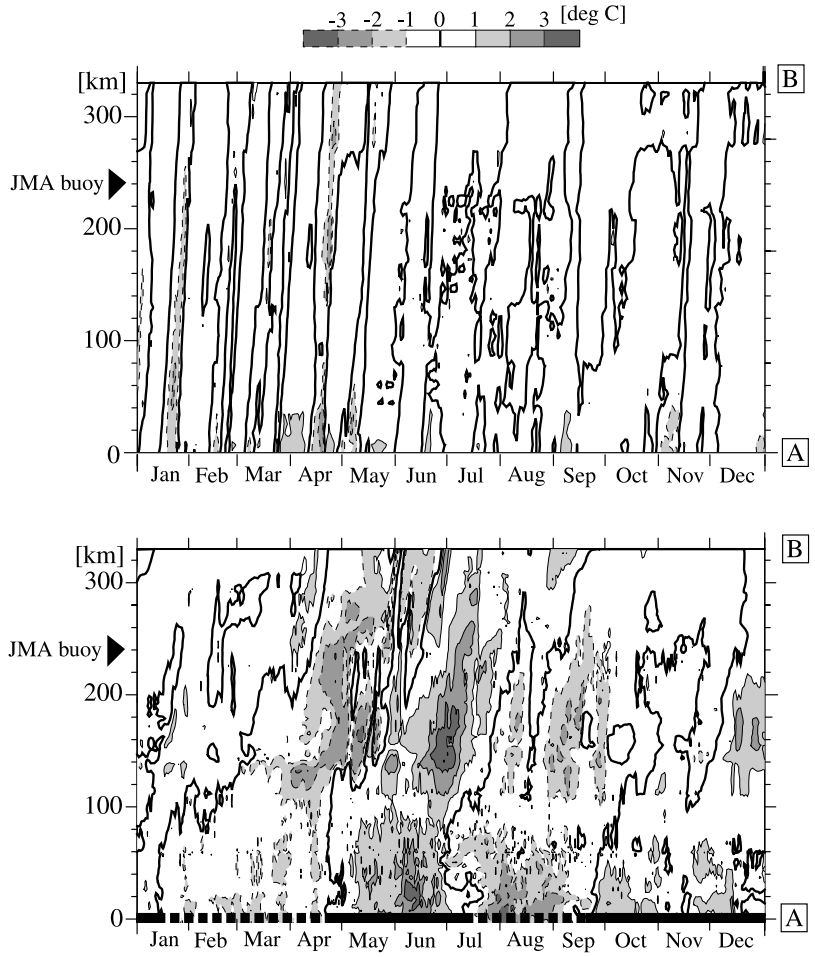

Figure 8. Space-time plot of the temperature anomaly at 10-m depth along 200-m isobath between points *A* and *B* in the top panel of Figure 7. The temperature anomaly processed in the top panel of Figure 7 is used to depict this figure. Contour interval is 1°C. Dashed lines are used for negative values. The top panel denotes the space-time plot along the same line in Region 1. In the bottom panel for Region 2, the positive and negative phases at point *A* are represented by solid and dashed lines, respectively. The location of the JMA buoy station is indicated by the solid triangle.

gradually as they propagate downstream along the shelf break. In addition, the distribution pattern suggests that large RMS results from activities of Kuroshio branch [*Katoh et al.*, 2000] and mesoscale eddies in the downstream portion. The large RMS appears near the areas (see two large arrows in the top panel of Figure 7) where the bottom slope changes abruptly at the shelf break. The bottom panel of Figure 7 shows the observed RMS distribution computed with the data set used to depict Figure 6. In total, the observed values are larger than modeled values presumably owing to disturbances excluded from the present model (e.g., short-term meteorological fluctuations). However, the areas with large RMS (>1.2) are revealed at the same locations as the model (see two large arrows). In addition, as the distribution pattern in the model, the areas with large RMS broaden in the Kuroshio downstream direction.

[27] Figure 8 represents space-time plots of the temperature anomaly at 10-m depth along the 200-m isobath between points *A* and *B* (see the top panel of Figure 7 for their locations). The top panel of Figure 8 shows the space-time plot of the anomaly in Region 1 along the same line, while the bottom panel is the plot for Region 2. Although temperature fluctuations propagate downstream in Region 1, their magnitude are considerably weaker than results in Region 2. In addition to periodicity less than 1 month, the semiannual (in strict terms, 4- or 5-month) fluctuations are visible only in Region 2. For the reader's reference, the positive and negative phases in the semiannual cycle at point *A* are indicated by solid and dashed lines in the bottom panel of Figure 8.

[28] Temperature fluctuations with different periods seem to coexist in the space-time plot of Region 2, so that these fluctuations are decomposed into two complex EOF modes (see *Barnett* [1983] for its procedure) which account for more than 80% of the total signal. The first mode shown in the top panel of Figure 9 represents the semiannual variation clearly, while the second mode corresponds to fluctuations with period shorter than one month. The propagation speed of the second mode is variable in the range between 5 and 20 cm/s, which is consistent with the phase speed of Kuroshio frontal waves observed in the East China Sea

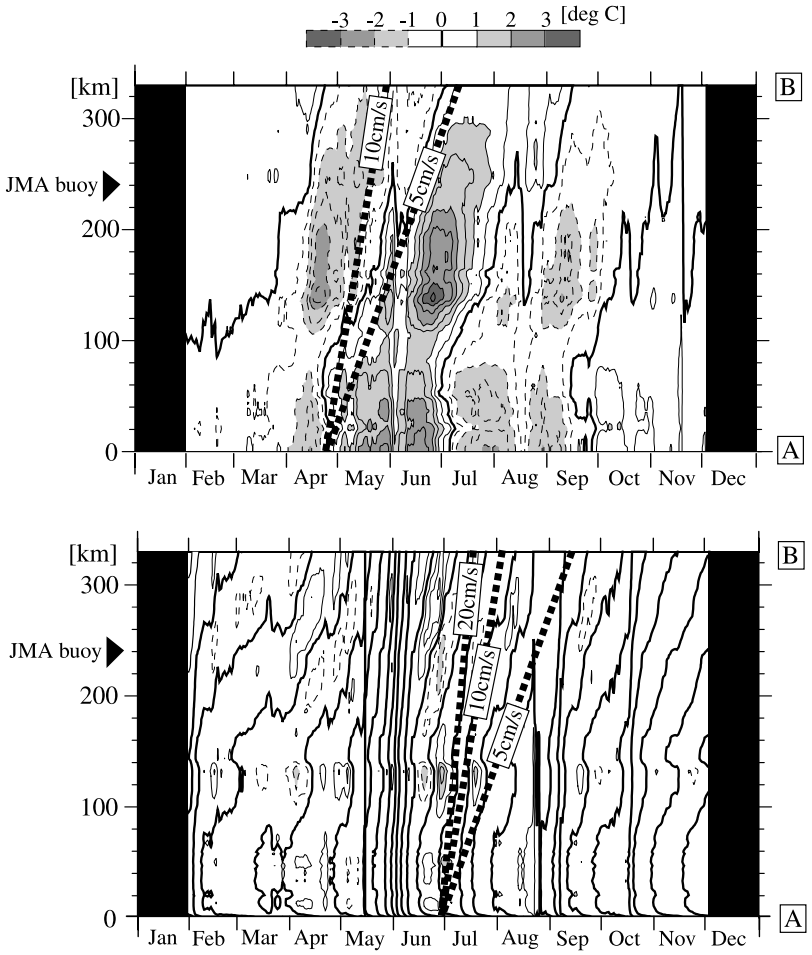

Figure 9. Space-time plot of the (top) first and (bottom) second modes of the complex EOF analysis adopted to the bottom panel of Figure 8. Contour interval is 1°C. Dashed lines are used for negative values. Data at both ends are omitted through the complex EOF analysis. Propagation speeds of 5, 10, and 20 cm/s are indicated by bold dashed lines for reference. The location of the JMA buoy station is indicated by the solid triangle.

(Table 1). The propagation speed of the first mode varies between 5 and 10 cm/s.

[29] Time series of model temperature at the buoy station are depicted in Figure 2 using results at 20-m depth in Regions 1 and 2. The Region 1 temperature fluctuations do not persist throughout the year, while the Region 2 fluctuations with periods shorter than one month do exist throughout the year. In addition, the amplitudes of the Region 2 fluctuations reach 1–2°C which agrees with observation. Thus we conclude that eddy activity including Kuroshio frontal waves and semiannual variation is reproduced realistically in Region 2. In the following section, we describe the temperature fields associated with fluctuations mentioned above, and evaluate the onshore cross-frontal transport in Region 2.

5. Discussion

5.1. Semiannual Variation

[30] Before estimating the cross-frontal transport at the shelf break, we first describe why the semiannual variation is seen at the JMA buoy station in Region 2. Figure 10 shows 10-m FVCOM temperature fields averaged over May, June, July and August. To show the semiannual variation clearly, we remove the annual average, the annual variation by fitting a sinusoidal curve, and short-term disturbances through a 5-day running mean.

[31] Figure 10 enables us to specify the area where the semiannual variation is generated. In May, a positive anomaly is created near point *A* where the bottom slope changes abruptly, the stable cyclonic eddy exists (Figure 5), and RMS temperature variability is large (Figure 7). The positive anomaly propagates downstream from May to June. Thereafter, a negative anomaly is created near point *A* in July, which then propagates downstream in August like the positive anomaly did two months before. The above process results in the semiannual variation revealed at the buoy station.

[32] According to the recent theoretical study by *Isobe* [2004], frontal waves at the shelf break excite alternating bands of mean currents over the shelf, and excite fluctuations with periods of several months. The semiannual variation may result from nonlinear interaction between frontal and topographic Rossby waves as mentioned by

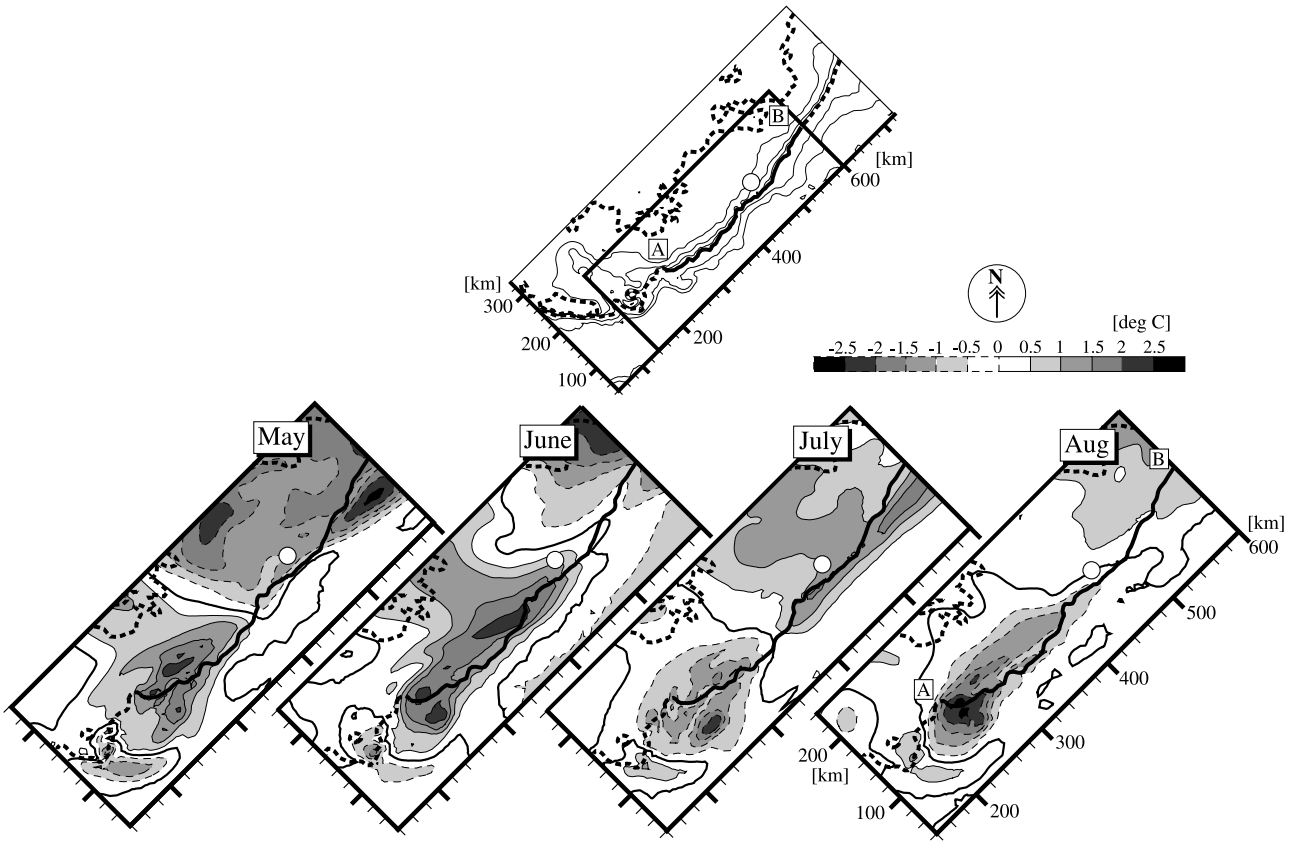

Figure 10. Horizontal distribution of the temperature anomaly averaged in May, June, July, and August at 10-m depth. The annual mean and annual variation are removed at each node. The area within the rectangle in the upper panel is enlarged in bottom four panels. Contour interval is 0.5°C. Dashed lines are used for the negative value. The 100- and 200-m isobaths are depicted in bottom four panels with bold lines. Points *A* and *B* are also shown in the panel for August as well as the top panel. The open circle denotes the JMA buoy station.

Isobe [2004] although in-depth examination of the modeled current field is needed to determine the exact dynamical nature of the semiannual fluctuations.

5.2. Kuroshio Frontal Waves and Their Related Cross-Frontal Transport

[33] Model temperature fluctuations suggesting the passage of Kuroshio frontal waves are observed throughout the year along the shelf break in Region 2. We present next two examples of growing frontal waves and their related cross-frontal transport.

[34] Figure 11 represents the horizontal distribution of temperature at 10-m depth within rectangles *A* and *B*; see the top right panel for their location. The first example occurs in rectangle *A* from June 18 to 24. A Kuroshio frontal wave takes the form of a folded-wave pattern on June 18. This wavy pattern has a spatial scale of about 200 km. A warm filament thereafter extends southwestward from 20 to 22 June. The extended warm filament detaches from the Kuroshio mainstream on 24 June, and moves onto the shelf. These four sequential panels demonstrate that an onshore transport can be induced intermittently by a breaking Kuroshio frontal wave. A similar transport process can be found within rectangle *B* from 18 to 24 March; see the top four panels. The spatial scale of this wavy pattern is about half compared to the wave in rectangle *A*. This second example indicates that eddy-induced onshore transports occur in various areas and various spatial scales.

[35] Onshore transports induced by Kuroshio frontal waves occur in the lower layer as well as the upper layer. Figure 12 shows the temperature distribution above the bottom (i.e., the deepest σ-layer) beneath the second example of Figure 11. Bold lines in Figure 12 represent the frontal wave detected at 10-m depth. As the frontal wave grows in the upper layer, offshore cold water advances onto the shelf, especially at the trough of the frontal wave in the lower layer; we herein call the portion where onshore (offshore) water extends offshore (onshore) the trough (crest). Figure 12 resembles the well-known schematic view of *Lee et al.* [1981, Figure 18] showing "upwelling" of offshore water at the trough of a Gulf Stream frontal wave over the outer shelf in the South Atlantic Bight. It is reasonable that offshore subsurface water is located at the trough of frontal waves because Kuroshio frontal waves are generated primary by baroclinic instability [*James et al.*, 1999], and because the phase of baroclinic instability waves in the lower layer is delayed in comparison to that in the upper layer. In addition to "upwelling" of offshore water, this vertical tilting of frontal waves results in the offshore intrusion of less saline shelf water into the Kuroshio

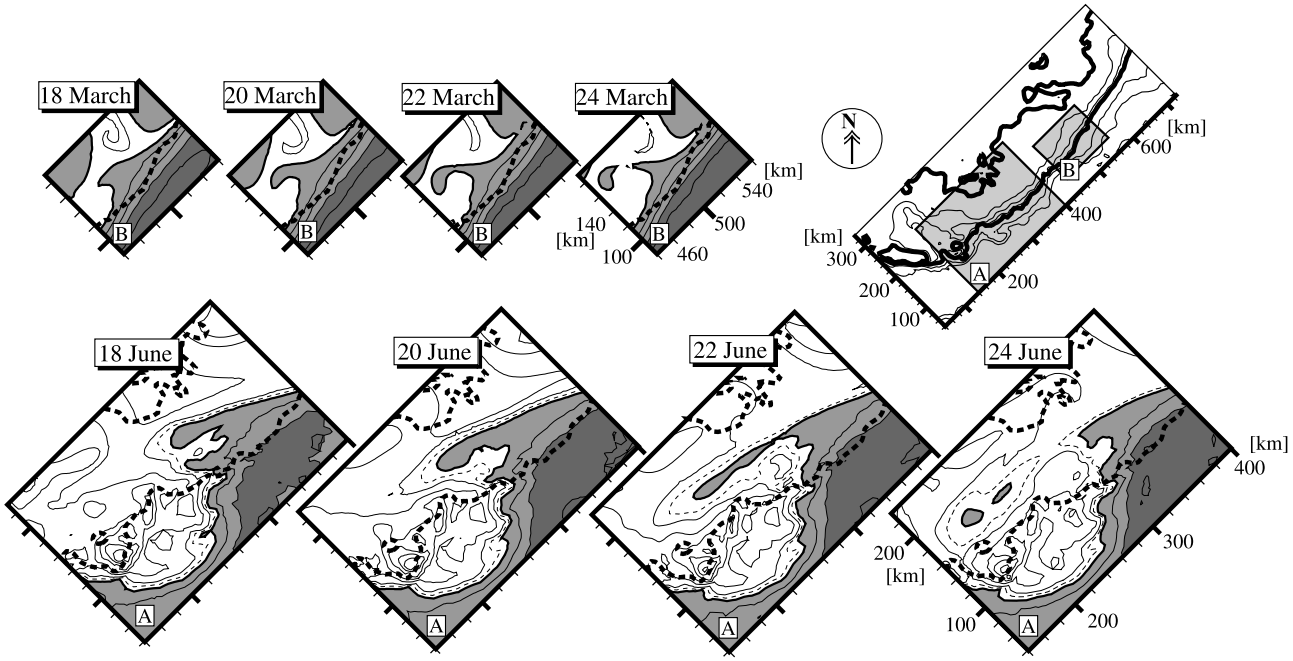

Figure 11. Horizontal distribution of temperature at 10-m depth from (top) 18 March to 24 March and (bottom) 18 June and 24 June. Areas within stippled rectangles *A* and *B* in the top right panel are enlarged in panels of June and March. Temperatures greater than 19°(26)°C are stippled in the March (June) panels to emphasize the folded-wave pattern of the frontal wave. In addition, contour lines of 25.5°C are shown in the June panels by thin dashed lines. The 100- and 200-m isobaths are depicted with bold dashed lines.

intermediate layer (not shown; we refer the reader to Figure 13 of *Isobe et al.* [2004]).

5.3. Estimate of the Onshore Transport at the Shelf Break in Region 2

[36] As shown in foregoing sections, periodicity and amplitude of temperature fluctuations are reproduced satisfactorily at the buoy station by FVCOM in Region 2. In addition, frontal waves propagate along the shelf break with phase speeds consistent with observations. Moreover, small-scale eddies are released from the Kuroshio onto the shelf when the frontal wave decays in the upper layer. The onshore subsurface intrusion of offshore water is also visible just beneath the trough of the frontal wave. We estimate the cross-frontal transport at the shelf break in conjunction with passive tracer experiments carried out in this numerical model.

[37] A passive tracer with the concentration of 1.0 is fixed along the 200-m isobath (i.e., the shelf break) in the course of the calculation. The tracer is set to be homogeneous vertically so that the tracer takes the form of a curtain at the shelf break. The tracer experiment is carried out using the current field from the final simulation year. Tracers leaving open boundaries never return to the model interior. Over the shelf shallower than 200-m depth, we calculate the total amount of tracer concentration multiplied by each cell volume, that is, the total amount of water including the passive tracer. Moreover, tracer leaving the open boundary where the water depth is less than 200 m (i.e., open boundaries over the shelf) is added to this estimate. Then

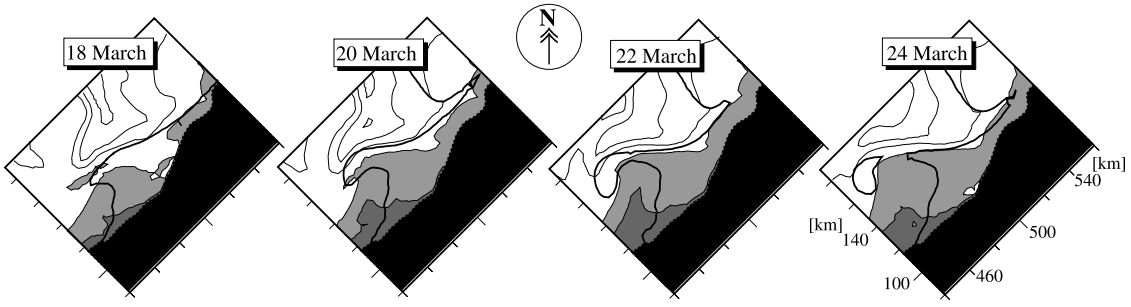

Figure 12. Horizontal distribution of temperature in the deepest σ layer within the rectangle *B* of Figure 11. Contour interval is 0.5°C. Stippling indicates temperatures less than 13°C; dense stippling indicates temperatures less than 12.5°C. Bold solid lines denote the 19°C isotherm at 10-m depth. Isotherm lines are omitted in the offshore region deeper than 200 m because of over crowding; note that the depth of the deepest σ layer is considerably different beyond the shelf break.

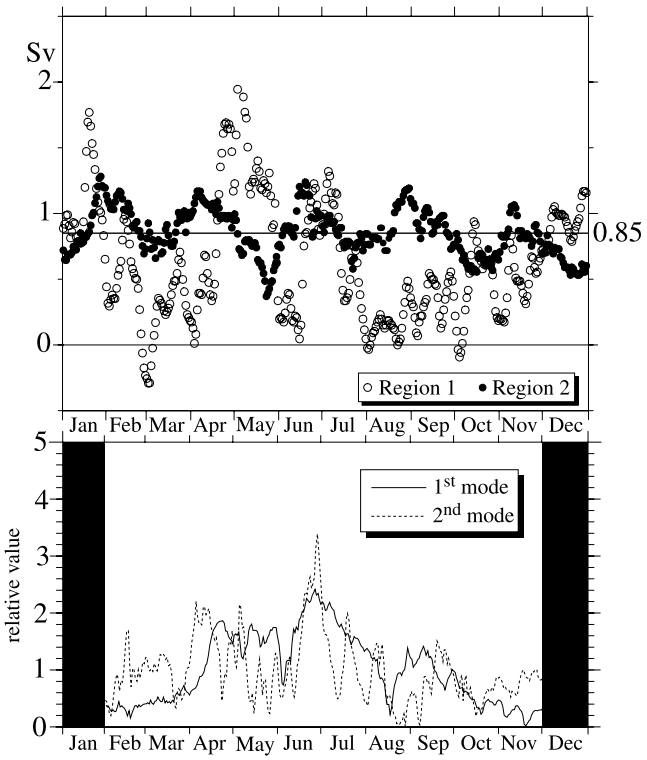

Figure 13. Results of tracer experiments. The top panel shows the onshore volume transports from the shelf break (i.e., 200-m isobath) estimated daily in the final simulation year. Solid (open) circles denote transports estimated in Region 2 (Region 1). Also shown is the annual mean (0.85 Sv) in Region 2. The bottom panel shows the temporal amplitude function of the first and second modes of the complex EOF analysis in section 4.2.

the time derivative of the total amount of water including the passive tracer is computed. Hence this time derivative is regarded as the net transport integrated along the shelf break of the model. When this transport is positive, a net onshore transport occurs from the Kuroshio region onto the shallow shelf. The above experiment is conducted in Region 1 as well as Region 2 for comparison of models with and without realistic frontal waves. The experiments exclude the horizontal diffusivity of tracer because the two models with different grid spacing have different horizontal diffusivities. However, when we add horizontal diffusivity in the model, the difference is negligible in the estimate of the onshore cross-frontal transport (not shown).

[38] The top panel of Figure 13 represents onshore transports of Regions 1 and 2 throughout the final year. Values in both Regions 1 and 2 are mostly positive, which means onshore transports occurred throughout the year. However, onshore transport varies largely in time in Region 1. Although transports in Region 1 exceed those in Region 2 sporadically, onshore transports take relatively small values, less than 0.5 Sv during much of the year. With realistic eddy activity, Region 2 exhibits stable onshore transports throughout the year, with an annually averaged onshore transport of 0.85 Sv.

[39] The temporal variation with the period of about three months is revealed in the onshore transport in Region 2. The bottom panel of Figure 13 shows the temporal amplitude function of the complex EOF analysis adopted to temperature fluctuations along the shelf break in Region 2 (see subsection 4.2 and Figure 9). The amplitude function represented by the solid (dashed) curve indicates activity of the first (second) mode of the fluctuations. Large onshore transport appears when the amplitude function of the second (frontal eddy) mode is large. This suggests that the onshore transport is induced primary by frontal waves along the shelf break.

[40] The solid line in Figure 14 represents the vertical profile of the annually averaged onshore transport per unit depth at the shelf break of Region 2. The transport decreases in the lower layer, presumably owing to bottom friction. Also shown in Figure 14 is the cumulative onshore transport integrated from the bottom. To put this into perspective, note that the cumulative transport in the deepest layer (25-m thickness) reaches nearly the same transport as the Changjiang river discharge (0.03 Sv). Furthermore, the cumulative transport in the bottom 100-m-thick layer exceeds 10 times this river discharge.

6. Conclusion

[41] It is reasonable to consider that growing Kuroshio frontal waves enhance the cross-frontal transport at the shelf break in the East China Sea. The goal of this study is to estimate the onshore cross-frontal transport integrated along the shelf break. However, it is difficult to estimate this transport only on the basis of field measurements because of intense spatiotemporal variability in eddy activity. Hence we use a numerical model approach in which characteristics (phase speed, period, and amplitude at the JMA buoy station) of Kuroshio frontal waves are reproduced realisti-

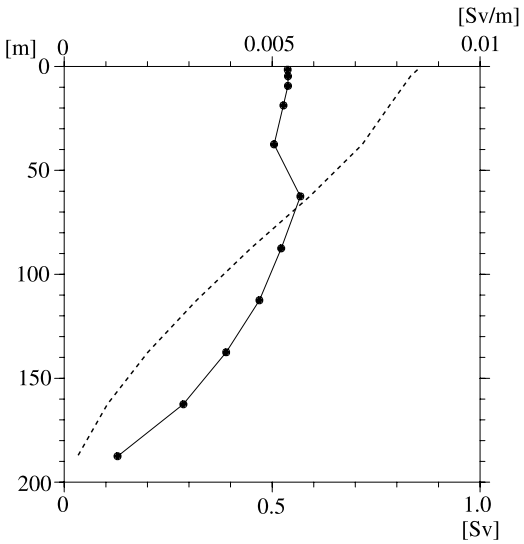

Figure 14. Vertical profile of the annually averaged onshore transport at the shelf break in Region 2. The solid line shows the transport per unit depth; see the upper abscissa for this value. Dots represent the mid-depth of each σ layer. The dashed line represents the cumulative onshore volume transport integrated from the bottom; see the lower abscissa for this value.

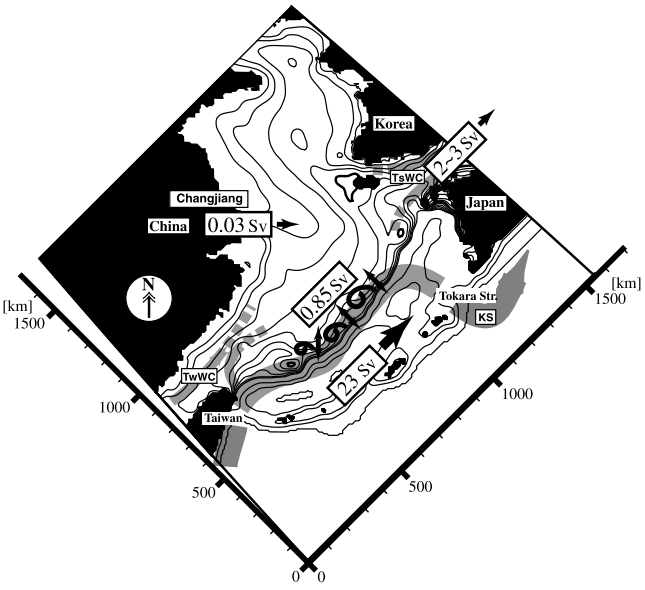

Figure 15. Annually averaged volume transports of Kuroshio [*Ichikawa and Chaen*, 2000], Tsushima Warm Current [*Isobe et al.*, 2002; *Teague et al.*, 2002; *Takikawa et al.*, 2005], Changjiang river discharge [*Shen et al.*, 1998], and the onshore transport at the shelf break in Region 2.

cally. One advantage of this study is that we use the unstructured triangular grid of FVCOM to resolve the complex shelf break bottom topography that may trigger frontal waves. In fact, Kuroshio frontal waves are generated in FVCOM around the location where the shelf break bottom slope changes abruptly over small scales, and have phase speeds and amplitudes consistent with those observed in the East China Sea. In addition to the complex bottom topography, the high-resolution FVCOM can reproduce the horizontal velocity shear that also triggers frontal waves [*Zheng and Yuan*, 1986]. It is anticipated that these frontal waves exchange seawater between the Kuroshio and shelf regions. On the basis of passive tracer experiments with FVCOM, the annually averaged onshore-transport integrated along the shelf break is estimated to be 0.85 Sv. This is shown schematically in Figure 15 together with various volume transports to be compared with this onshore transport.

[42] Ocean currents over the shelf are directed toward the Tsushima/Korea Strait [*Katoh et al.*, 2000], and are called the Tsushima Warm Current after passing the strait. Recent observations have estimated the volume transport of the Tsushima Warm Current to be between 2 and 3 Sv [*Isobe et al.*, 2002; *Teague et al.*, 2002; *Takikawa et al.*, 2005]. The amount (0.85 Sv) of saline Kuroshio water mixed at the shelf break reaches 30–40% of this volume transport. We therefore conclude that Kuroshio frontal waves play a significant role in the water mass formation of the Tsushima Warm Current, and that the onshore transport at the shelf break is one source of Tsushima Warm Current water. This thought is consistent with *Lim* [1971] and *Sawara and Hanzawa* [1979] who consider that Tsushima Warm Current water originates from the shelf break of the East China Sea through mixture between Kuroshio and less saline shelf waters.

[43] There are two major nutrient sources in the Yellow and East China seas. One is the Changjiang, with an annually averaged discharge (0.03 Sv) that accounts for about 90% of the total river discharge into this area. Recently, on the basis of a nutrient budget in this area, *Chen and Wang* [1999] point out that the nutrient supply from the Kuroshio subsurface layer is much larger than that from the Changjiang. As shown in Figure 14, the onshore transport from the Kuroshio just in the deepest layer (25-m thickness) of the model is comparable with the Changjiang river discharge. The nutrient transport should be quantified with numerical models that include ecosystem processes as well as realistic eddy activity over the shelf break. This initial study suggests that the nutrient supplied by the Kuroshio subsurface layer is likely to be an important fraction in the overall nutrient budget of this area.

[44] **Acknowledgments.** The authors express their sincere thanks to Changsheng Chen, Geoffrey Cowles, and Hector Sepulveda for their helpful advice in modeling with FVCOM. The original manuscript was improved through the helpful comments of two reviewers. This study was carried out when A. I. stayed at WHOI with the grant of Overseas Advanced Educational Research Practice Support Program supported by the Ministry of Education, Science and Culture, Japan. In addition, the Japan Society for the Promotion of Science supported this study through Grant-in-Aid for Scientific Research.

References

Barnett, T. P. (1983), Interaction of the monsoon and Pacific Trade Wind system at interannual time scales: I. The equatorial zone, *Mon. Weather Rev.*, *111*, 756–773.

Boyer, T., and S. Levitus (1994), Quality control and processing of historical oceanographic temperature, salinity, and oxygen data, *NOAA Tech. Rep. NESDIS 81*, 38 pp., Natl. Oceanic and Atmos. Admin., Silver Spring, Md.

Chang, P.-H., and A. Isobe (2003), A numerical study on the Changjiang Diluted Water in the East and Yellow China seas, *J. Geophys. Res.*, *108*(C9), 3299, doi:10.1029/2002JC001749.

Chen, A. C.-T., and S.-L. Wang (1999), Carbon, alkalinity and nutrient budgets on the East China Sea continental shelf, *J. Geophys. Res.*, *104*(C9), 20,675–20,686.

Chen, C., R. C. Beardsley, R. Limeburner, and K. Kim (1994), Comparison of winter and summer hydrographic observations in the Yellow and East China Sea and adjacent Kuroshio during 1986, *Cont. Shelf Res.*, *14*, 909–929.

Chen, C., H. Liu, and R. C. Beardsley (2003), An unstructured grid, finite-volume, three-dimensional, primitive equations ocean model: Application to coastal ocean and estuaries, *J. Atmos. Oceanic Technol.*, *20*, 159–186.

Choi, B. H., K. O. Kim, and H. M. Eum (2002), Digital bathymetric and topographic data for neighboring seas of Korea (in Korean with English abstract and figure captions), *J. Korean Soc. Coastal Ocean Eng.*, *14*, 41–50.

Fang, G., B. Zhao, and Y. Zhu (1991), Water volume transport through the Taiwan Strait and the continental shelf of the East China Sea measured with current meters, in *Oceanography of Asian Marginal Seas*, edited by K. Takano, pp. 345–348, Elsevier, New York.

Hanawa, K., and H. Mitsudera (1985), On the data processing of daily mean values of oceanographic data: Note on the daily mean sea-level data (in Japanese), *Bull. Coastal Oceanogr.*, *23*, 79–87.

Hsueh, Y., H.-J. Lie, and H. Ichikawa (1996), On the branching of the Kuroshio west of Kyushu, *J. Geophys. Res.*, *101*(C2), 3851–3857.

Ichikawa, H., and R. C. Beardsley (1993), Temporal and spatial variability of volume transport of the Kuroshio in the East China Sea, *Deep Sea Res.*, *40*, 583–605.

Ichikawa, H., and M. Chaen (2000), Seasonal variation of heat and freshwater transports by the Kuroshio in the East China Sea, *J. Mar. Syst.*, *24*, 119–129.

Isobe, A. (1999a), On the origin of the Tsushima Warm Current and its seasonality, *Cont. Shelf Res.*, *19*, 117–133.

Isobe, A. (1999b), The Taiwan-Tsushima Warm Current System: Its path and the transformation of the water mass in the East China Sea, *J. Oceanogr.*, *55*, 185–195.

Isobe, A. (2000), Two-layer model on the branching of the Kuroshio southwest of Kyushu, Japan, *J. Phys. Oceanogr.*, *30*, 2461–2476.

Isobe, A. (2004), Driving mechanism of band structure of mean current over the continental shelf, *J. Phys. Oceanogr.*, *34*, 1839–1855.

Isobe, A., M. Ando, T. Watanabe, T. Senjyu, S. Sugihara, and A. Manda (2002), Freshwater and temperature transports through the Tsushima-Korea Straits, *J. Geophys. Res.*, *107*(C7), 3065, doi:10.1029/2000JC000702.

Isobe, A., E. Fujiwara, P.-H. Chang, K. Sugimatsu, M. Shimizu, T. Matsuno, and A. Manda (2004), Intrusion of less saline shelf water into the Kuroshio subsurface layer in the East China Sea, *J. Oceanogr.*, *60*, 853–863.

James, C., M. Wimbush, and H. Ichikawa (1999), Kuroshio meanders in the East China Sea, *J. Phys. Oceanogr.*, *29*, 259–272.

Katoh, O., K. Teshima, O. Abe, H. Fujita, K. Miyaji, K. Morinaga, and N. Nakagawa (1996), Process of the Tsushima Current formation revealed by ADCP measurements in summer, *J. Oceanogr.*, *52*, 491–507.

Katoh, O., K. Morinaga, and N. Nakagawa (2000), Current distributions in the southern East China Sea in summer, *J. Geophys. Res.*, *105*(C4), 8565–8573.

Large, W. G., and S. Pond (1981), Open ocean momentum flux measurements in moderate to strong winds, *J. Phys. Oceanogr.*, *11*, 324–336.

Lee, T. N., L. P. Atkinson, and R. Legeckis (1981), Observations of a Gulf Stream frontal eddy on the Georgia continental shelf, April 1977, *Deep Sea Res.*, *28*, 347–378.

Lie, H.-J., and C.-H. Cho (1994), On the origin of the Tsushima Warm Current, *J. Geophys. Res.*, *99*(C12), 25,081–25,091.

Lie, H.-J., C.-H. Cho, and J.-H. Lee (1998), Separation of the Kuroshio water and its penetration onto the continental shelf west of Kyushu, *J. Geophys. Res.*, *103*(C2), 2963–2976.

Lim, D.-B. (1971), On the origin of the Tsushima Warm Current Water, *J. Oceanol. Soc. Korea*, *6*, 85–91.

Mellor, G. L. (2003), Users guide for a three-dimensional, primitive equation, numerical ocean model (June 2003 version), report, 53 pp., Program in Atmos. and Oceanic Sci., Princeton Univ., Princeton, N. J.

Mellor, G. L., and T. Yamada (1982), Development of a turbulence closure model for geographical fluid problems, *Rev. Geophys.*, *20*, 851–875.

Qiu, B., T. Toda, and N. Imasato (1990), On Kuroshio front fluctuations in the East China Sea using satellite and in situ observational data, *J. Geophys. Res.*, *95*(C10), 18,191–18,204.

Sawara, T., and Y. Hanzawa (1979), Distribution of water type in the East China Sea (in Japanese with English abstract and figure captions), *Mar. Sci. Mon.*, *54*, 135–148.

Shen, H., C. Zhang, C. Xiao, and J. Zhu (1998), Change of the discharge and sediment flux to estuary in Changjiang River, in *Health of the Yellow Sea*, edited by G. H. Hong, J. Zhang, and B. K. Park, pp. 129–148, Earth Love Publ. Assoc., Seoul.

Sugimoto, T., S. Kimura, and K. Miyaji (1988), Meander of the Kuroshio front and current variability in the East China Sea, *J. Oceanogr. Soc. Jpn.*, *44*, 125–135.

Takikawa, T., J.-H. Yoon, and K.-D. Cho (2005), The Tsushima Warm Current through Tsushima Straits estimated from ferryboat ADCP data, *J. Phys. Oceanogr.*, *35*, 1154–1168.

Teague, W. J., G. A. Jacobs, H. T. Perkins, J. W. Book, K. I. Chang, and M. S. Suk (2002), Low-frequency current observations in the Korea/Tsushima Strait, *J. Phys. Oceanogr.*, *32*, 1621–1641.

Torrence, C., and G. P. Compo (1998), A practical guide to wavelet analysis, *Bull. Am. Meteorol. Soc.*, *79*, 61–78.

Uda, M. (1934), Hydrographical researches on the normal monthly conditions in the Japan Sea, the Yellow Sea, and the Okhotsk Sea (in Japanese), *J. Imp. Fish. Exp. Sta. Jpn.*, *5*, 191–236.

Woodruff, S. D., R. J. Slutz, R. L. Jenne, and P. M. Steurer (1987), A comprehensive ocean-atmosphere data set, *Bull. Am. Meteorol. Soc.*, *68*, 1239–1250.

Wu, C. R., and Y. C. Hsin (2005), Volume transport through the Taiwan Strait: A numerical study, *Terr. Atmos. Oceanic Sci.*, *16*, 377–391.

Yanagi, T., T. Shimizu, and H.-J. Lie (1998), Detailed structure of the Kuroshio frontal eddy along the shelf edge of the East China Sea, *Cont. Shelf Res.*, *18*, 1039–1056.

Zhao, B.-R., and G.-H. Fang (1991), The estimate of transport of the main water route in the East China Sea, *Acta Oceanol. Sin.*, *13*, 169–178.

Zheng, Q.-N., and Y.-L. Yuan (1986), Intermediate-scale wave motion in shallow-water shear current, *J. Geophys. Res.*, *91*(C3), 3959–3965.

R. C. Beardsley, Physical Oceanography Department, Woods Hole Oceanographic Institution, MS21, Woods Hole, MA 02543, USA.

A. Isobe, Department of Earth System Science and Technology, Interdisciplinary Graduate School of Engineering Sciences, Kyushu University, 6-1, Kasuga-Koen, Kasuga, 8168580, Japan. (isobe@esst.kyushu-u.ac.jp)